OPEN ACCESS
JOURNAL OF ADVANCED DIELECTRICS
Vol. 11, No. 2 (2021) 2150013 (8 pages)

DOI: 10.1142/S2010135X21500132

# Impedance and modulus studies of $Na_{0.9}Ba_{0.1}Nb_{0.9}(Sn_{0.5}Ti_{0.5})_{0.1}O_3$ ceramic

A. Oueslati* and A. Aydi†,‡

*Laboratory of Spectroscopic Characterization and Optical Materials
Faculty of Sciences, University of Sfax
B.P.1171, 3000 Sfax, Tunisia

†Laboratory of Multifunctional Materials and Applications (LaMMA)
LR16ES18, Faculty of Sciences of Sfax, University of Sfax
BP 1171, 3000 Sfax, Tunisia

‡aydi_abdelhedi@yahoo.fr

Received 24 February 2021; Revised 8 April 2021; Accepted 13 April 2021; Published 6 May 2021

Polycrystalline $Na_{0.9}Ba_{0.1}Nb_{0.9}(Sn_{0.5}Ti_{0.5})_{0.1}O_3$ is prepared by the solid-state reaction technique. The formation of single-phase material was confirmed by an X-ray diffraction study and it was found to be a tetragonal phase at room temperature. Nyquist plots ($Z''$ versus $Z'$) show that the conductivity behavior is accurately represented by an equivalent circuit model which consists of a parallel combination of bulk resistance and constant phase elements (CPE). The frequency dependence of the conductivity is interpreted in terms of Jonscher's law. The conductivity $\sigma_{dc}$ follows the Arrhenius relation. The modulus plots can be characterized by the empirical Kohlrausch–Williams–Watts (KWW), $\varphi(t) = \exp(-(t/\tau)^{\beta})$ function and the value of the stretched exponent ($\beta$) is found to be almost independent of temperature. The near value of activation energies obtained from the analyses of modulus and conductivity data confirms that the transport is through an ion hopping mechanism dominated by the motion of the ($O^{2-}$) ions in the structure of the investigated material.

*Keywords*: Ceramics; impedance spectroscopy; equivalent circuit; modulus; electrical conductivity.

## 1. Introduction

With high demand and rapid progress in the miniaturization of electrical components, considerable attention has been paid to the function and role of interfaces in electroceramics. These materials exhibit a variety of physical properties such as application in laser host,[1] ferroelectric/ferroelastic behavior,[2,3] ferromagnetism,[4] anomalous semiconductor to metal transition,[5] spin-glass behavior,[6] ionic conductors,[7,8] and semiconductor.[9] These applications need a compound with high electrical conductivity and good thermal and chemical stability. In fact, many new solid solutions with excellent properties have been developed, such as $Ba_{1-x}$ $Sr_xTiO_3$,[10] $BaTi_{1-x}$ $Sn_xO_3$,[11,12] and $NaNbO_3$[13] ceramics. As an element of this group, the present work selected $Na_{0.9}Ba_{0.1}Nb_{0.9}(Sn_{0.5}Ti_{0.5})_{0.1}O_3$ material for investigation. It crystallizes in the tetragonal structure.[14] Electrical conduction in these materials has contributions from grains (bulk), grain boundaries, and electrode specimen interface.[15] To understand the conduction behavior, it is necessary to separate various contributions to the total observed resistance. Complex impedance spectroscopy is an important and powerful tool to study defects, microstructure, surface chemistry, and electrical properties of materials. In the present research work, we have prepared $Na_{0.9}Ba_{0.1}Nb_{0.9}$ $(Sn_{0.5}Ti_{0.5})_{0.1}O_3$ ceramic by a solid-state synthesis. By designing an electrical equivalent circuit, we tried to explain the electrical conduction and relaxation mechanism.

## 2. Experimental Procedure

The polycrystalline ceramics sample of $Na_{0.9}Ba_{0.1}Nb_{0.9}$ $(Sn_{0.5}Ti_{0.5})_{0.1}O_3$ was prepared by a conventional standard solid-state synthesis. The appropriate stoichiometric ratio of the precursors ($BaCO_3$, $Na_2CO_3$, $Nb_2O_5$, $TiO_2$, and $SnO_2$) of high purity (99.9%) were weighted and initially mixed in an agate mortar in order to make a homogenous mixture of the ingredients for 1 h. Then the powder was calcined in air at 1300 K for 12 h. After calcination, the powder was pressed into pellets of 8 mm diameter and 1.6 mm thickness using 3 t/cm$^2$ uniaxial pressure. These pellets have been sintered at 1523 K for 2 h in the air atmosphere.

The material formation was confirmed by an X-ray diffraction study. XRD pattern of the material was recorded at room temperature using a Phillips powder diffractometer PW 1710 with $CuK_{\alpha}$ radiation ($\lambda = 1.5419$ Å) in a wide range of Bragg angles ($5° \leq 2\theta \leq 80°$). Unit cells parameters of the

‡Corresponding author.

synthesized compound have been refined by the least square method from the powder data.

The microstructure of the compound was imaged using scanning electron microscopy (SEM, JSM EMP-2300).

The sintered pellet was used for electrical conductivity measurements. The metallization by a gold layer of the two parallel surfaces of this pellet made it possible to carry out studies of electrical conductivity. The ac conductivity measurements were performed with a Tegam 3550 impedance analyzer (200 Hz–5 MHz) which was also interfaced with a computer and a temperature controller. Measurements were carried out at temperatures from 450 K to 723 K. The temperature of the sample was measured with the aid of a copper-constant a thermocouple placed near the sample.

Complex impedance data, $Z^*$, can be represented by its real, $Z'$, and imaginary, $Z''$, parts by the relation $Z^* = Z' - iZ''$.

## 3. Results and Discussion

### 3.1. *Powder X-ray analysis*

The room temperature powders X-ray diffractogram of the $Na_{0.9}Ba_{0.1}Nb_{0.9}$ $(Sn_{0.5}Ti_{0.5})_{0.1}O_3$ compound is shown in Fig. 1. All the reflection peaks were indexed in the tetragonal symmetry with the P4mm space group. The refined lattice parameters are $a$ = 3.918(8) Å and $c$ = 3.928(1) Å, and $V$ = 391.577(4) Å$^3$ with an estimated standard deviation in parenthesis. The unit cell parameters are in good agreement with the literature values.[1]

### 3.2. *Impedance analysis and equivalent circuit*

Impedance spectroscopy is a useful method to resolve the contributions of various processes such as bulk, grain boundary, and electrode effect in the specified frequency domain. In addition, the resistance and the capacitance associated with the solids could be estimated using impedance spectroscopy.

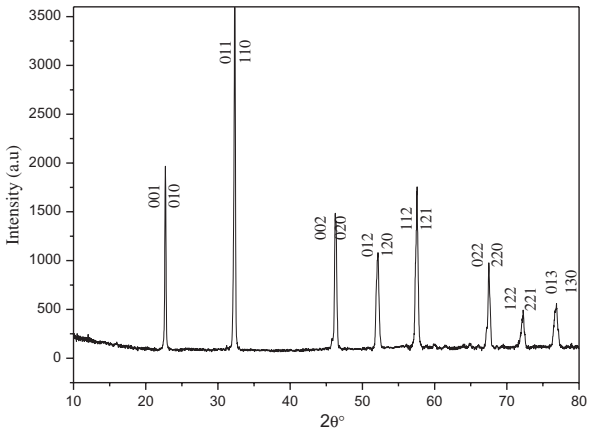


Fig. 1. X-ray diffraction pattern of $Na_{0.9}Ba_{0.1}Nb_{0.9}$ $(Sn_{0.5}Ti_{0.5})_{0.1}O_3$ ceramic sample.

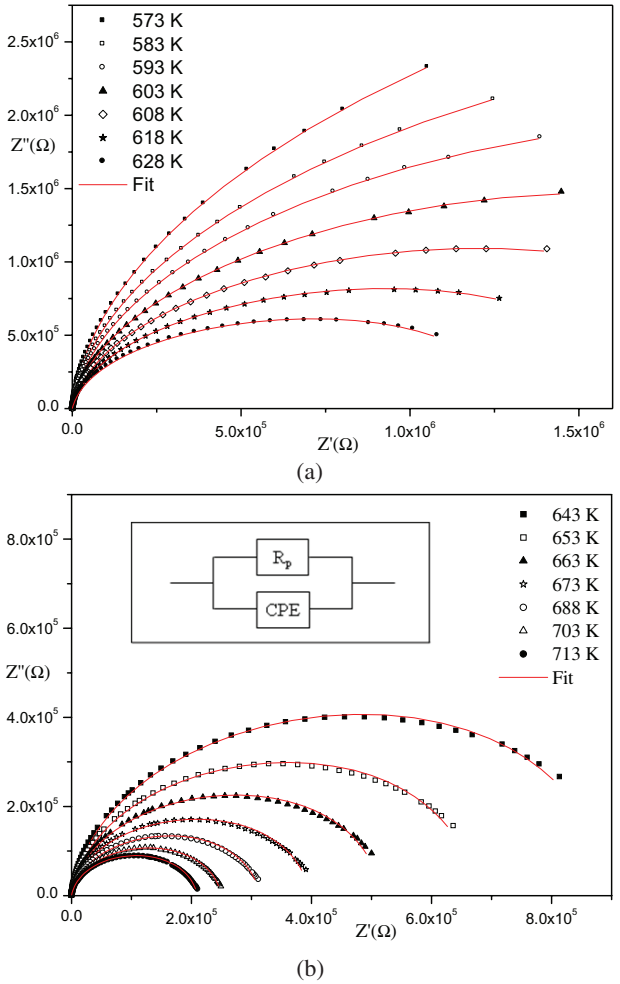


Fig. 2. (a) and (b): Complex impedance plots (measured and calculated) of $Na_{0.9}Ba_{0.1}Nb_{0.9}$ $(Sn_{0.5}Ti_{0.5})_{0.1}O_3$ ceramic at different temperatures.

The Nyquist plots (imaginary part of complex impedance $Z''$ versus real part of complex impedance $Z'$) of impedance data of $Na_{0.9}Ba_{0.1}Nb_{0.9}$ $(Sn_{0.5}Ti_{0.5})_{0.1}O_3$ at several temperatures are shown in Figs. 2(a) and 2(b). The plots are characterized by the appearance of semicircle arcs whose pattern changes, but not their shape, when the temperature is raised. The center of these semicircles is depressed below the real axis, indicating the non-Debye type of relaxation process.[16] The best fits are obtained when we use an equivalent circuit in evolving a resistance $R_b$ (bulk resistance) and constant phase element (CPE). Figure 3 shows the equivalent circuit. The impedance $Z_{CPE}$ is given by the relationship:

$$Z_{CPE} = \frac{1}{Q(j\omega)^{\alpha}}, \quad (1)$$

where $\alpha$ $(0 < \alpha < 1)$ is the measure of the capacitive nature of the element[17]: if $\alpha = 1$, the element is an ideal capacitor and if $\alpha = 0$, it behaves as a frequency-independent ohmic

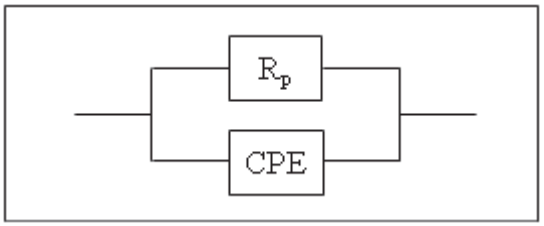


Fig. 3. Equivalent circuit model of the $Na_{0.9}Ba_{0.1}Nb_{0.9}(Sn_{0.5}Ti_{0.5})_{0.1}O_3$ compound.

resistor. $Q$ is the CPE parameter (expressed in Farad units). The expression of real ($Z'$) and imaginary ($-Z''$) components of impedance related to the equivalent circuit is

$$Z' = \frac{R_b^2 Q\omega^{\alpha}\cos(\alpha\pi/2) + R_b}{(1 + R_b Q\omega^{\alpha}\cos(\alpha\pi/2))^2 + (R_b Q\omega^{\alpha}\sin(\alpha\pi/2))^2}, \quad (2)$$

$$-Z'' = \frac{R_b^2 Q\omega^{\alpha}\sin(\alpha\pi/2)}{(1 + R_b Q\omega^{\alpha}\cos(\alpha\pi/2))^2 + (R_b Q\omega^{\alpha}\sin(\alpha\pi/2))^2}. \quad (3)$$

The parameters $R_b$, $Q$, and $\alpha$ have been obtained by using a mean square method that is used to minimize the difference between the experimental and calculated data.

In Fig. 4, we show the experimental and calculated values of $Z'$ as a function of $\omega$ using the equivalent circuit. The decrease in $Z'$ with a rise in temperature and frequency indicates the possibility of an increase in the ac conductivity with an increase in temperature and frequency.[18] All the curves merge in the high-frequency region ($>10^5$ Hz), and then $Z'$ becomes independent of frequency. This may be attributed to the release of space charge at higher temperatures.[19,20] The angular frequency dependence of the experimental and simulated (solid line) of the imaginary part of impedance ($Z''$)

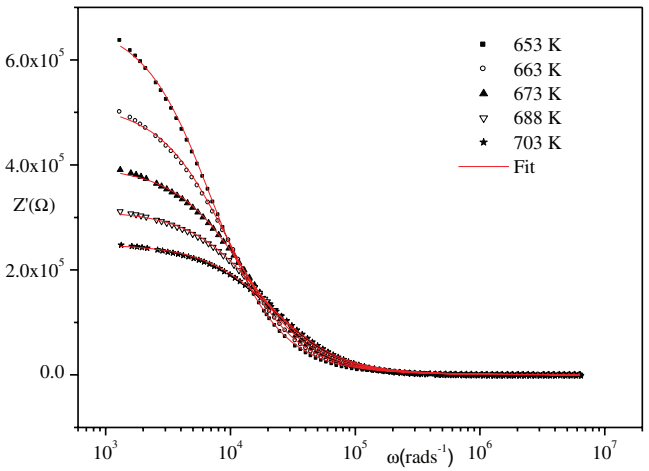


Fig. 4. Variation of real part of the impedance $Z'$ as a function of frequency.

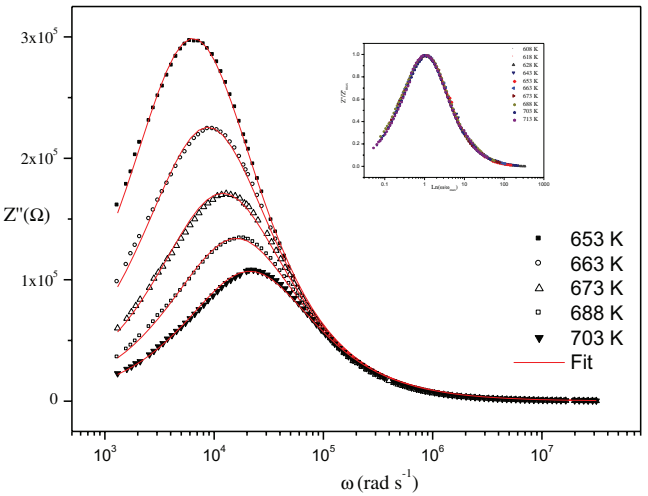


Fig. 5. Variation of imaginary part of the impedance $Z''$ as a function of frequency. Inset shows the scaling behavior of Im($Z''$).

at various temperatures is shown in Fig. 5. The nature of variation of $Z''$ with frequency is characterized by (a) the appearance of peaks at a particular frequency, (b) a decrease in the height of the peaks with a rise in temperature, (c) significant broadening of the peaks with a rise in temperature, (d) marked asymmetry in the peak pattern, and (e) merger of the spectrum at higher frequencies irrespective of temperature.[21,22] All these characteristics mainly indicate the temperature dependency of relaxation time. The frequency range of this relaxation suggests that relaxation is due to the free charges (ions, electrons, oxygen vacancies, etc.) which are trapped in intergrain space and electrode–electrolyte interface. The scaling has been attempted with the imaginary part of impedance ($Z''$) data as shown in Fig. 5 (inset). The $Z''$ plots at different temperatures overlap on a single master curve indicating that the dynamical process occurring at different frequencies has the same thermal activation energy,[23] which could be interpreted to mean there is no temperature dependence of conductivity.

Nyquist plots reported in Figs. 2, 4, and 5 show a good agreement between theoretical and experimental data. Fitted values of $R_b$, $Q$, and $\alpha$ parameters for different temperatures are listed in Table 1. It is obvious that all the capacitance values ($Q$) are in the range of pF. This implies that the single semicircular response is from grain interiors, which is expected from the sample where no grain boundaries are involved. The values of $\alpha$ vary in the range 0.86–0.96 confirming the weakness interaction between localized sites. The electrical conductivity can be obtained from

$$\sigma_b - \frac{h}{R_b S}, \quad (4)$$

where $h$ and $S$ are the thickness and cross-sectional area of the pellet, respectively. The temperature dependence of the

Table 1. Resulting parameters of each fitting corresponding to the equivalent circuits of Fig. 3.

| Temperature (K) | $R_b$ (ohms) | $Q$ (Farad) | $\alpha$ |
|---|---|---|---|
| 573 | 4.32E+06 | 7.31E-12 | 0.961 |
| 583 | 3.68E+06 | 7.07E-12 | 0.956 |
| 593 | 3.37E+06 | 5.91E-12 | 0.951 |
| 603 | 2.72E+06 | 5.90E-12 | 0.945 |
| 608 | 2.17E+06 | 4.00E-12 | 0.937 |
| 618 | 1.69E+06 | 4.12E-12 | 0.931 |
| 628 | 1.31E+06 | 4.35E-12 | 0.921 |
| 643 | 8.99E+05 | 4.64E-12 | 0.912 |
| 653 | 6.75E+05 | 4.88E-12 | 0.905 |
| 663 | 5.17E+05 | 3.55E-12 | 0.901 |
| 673 | 3.98E+05 | 3.24E-12 | 0.898 |
| 688 | 3.14E+05 | 3.21E-12 | 0.895 |
| 703 | 2.50E+05 | 3.09E-12 | 0.896 |
| 713 | 2.10E+05 | 2.86E-12 | 0.871 |
| 723 | 2.00E+05 | 2.31E-12 | 0.851 |

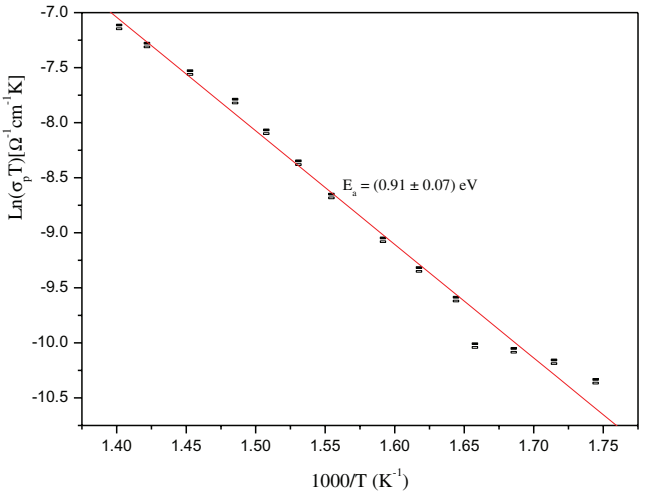


Fig. 6. Temperature dependence of the bulk conductivity.

conductivity is represented in Fig. 6 in the form of $\ln(\sigma_b T)$ versus $1000/T$. The linear behavior of electrical conductivity is in close agreement with the Arrhenius relation $\sigma_b T = A \exp(-E_a/k_B T)$, where $E_a = 0.91$ eV is the activation energy, $k_B$ is the Boltzmann constant, and $T$ is the absolute temperature.

### 3.3. *Ac conductivity analysis*

For analyzing the dynamic response of the material based on the alternating electric field, the study of experimental data has been done on the real part $\sigma'$ of the complex conductivity of the material $\sigma^*$, also known as ac conductivity ($\sigma_{ac}$).

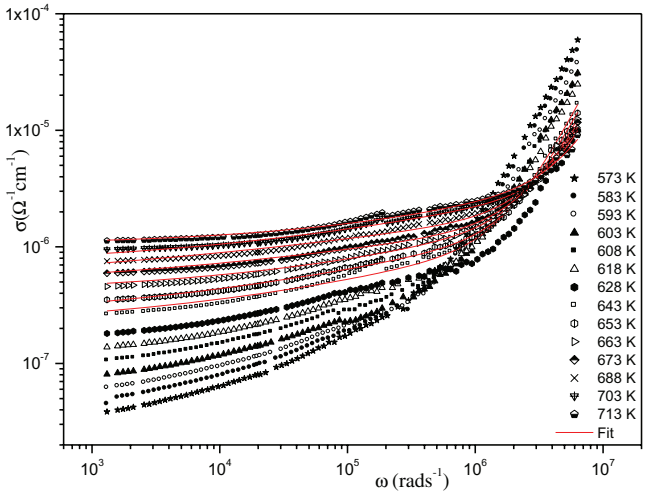


Fig. 7. Frequency dependence of the ac conductivity at various temperatures.

The angular frequency dependence of the ac conductivity at various temperatures for the sample is shown in Fig. 7. It is clear from the plot that the conductivity increases with the increase in frequency. From the previously mentioned figure, it is also evident that the dc contribution is important at low frequencies and high temperatures, yet in the low frequency region, the conductivity depends on temperature. Such dependence may be described by the variable range hopping mechanism,[24] which is frequency independent and only weakly temperature dependent compared with band theory. This model is important for the electrical conduction mechanism. This observed behavior was found to follow Johnscher's universal power law:

$$\sigma_{ac} = \sigma_{dc} + A\omega^n,$$

where $\sigma_{dc}$ is the direct current conductivity of the sample, $A$ is a constant for a particular temperature, and $n$ is the temperature-dependent exponent in the range of $0 \le n \le 1$. The exponent $n$ represents the degree of interaction between mobile ions with the lattices around them and the prefactor exponent $A$ determines the strength of polarizability.[25] Further rise in the conductivity value with temperature indicates that the electrical conduction in the material is a thermally activated process. These results agree well with the observations from impedance spectrum analysis. The variation of $\mathrm{Ln}(\sigma_{dc}T)$ versus $1000/T$ is shown in Fig. 8; it follows the Arrhenius relation with the activation energy $E_c = 0.94$ eV.

### 3.4. *Modulus analysis*

The complex modulus was introduced in this study to determine the parameters of the charge carrier and the relaxation time of the conductivity; it allows eliminating the problems related to the polarization of electrodes or other interfacial effects in the solid electrode.[26] Macedo *et al.*[27] formulated a

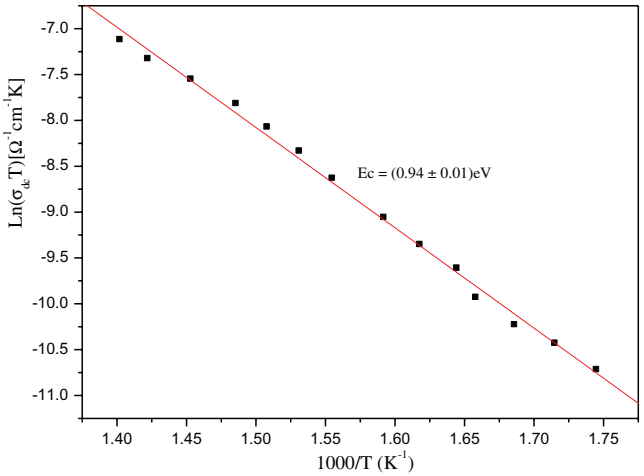


Fig. 8. Plot of DC conductivity $\sigma_{dc}$ versus 1000/$T$.

theory for conductivity relaxation in ion conductors in terms of a dimensionless quantity, $M^*$, which is defined as the inverse of complex permittivity, $\varepsilon^*(\omega)$. It is resolved into real and imaginary parts:

$$M^* = \frac{1}{\varepsilon'} = j\omega C_0 Z^* = M' + jM'', \tag{5}$$

$$M' = \frac{\varepsilon'}{(\varepsilon'^2 + \varepsilon''^2)}, \qquad M'' = \frac{\varepsilon''}{(\varepsilon'^2 + \varepsilon''^2)},$$

where $C_0 = \varepsilon_0 S/e$ is the vacuum capacitance of cell.

Figures 9(a) and 9(b) show the real $M'$ and imaginary parts $M''$ of the electrical modulus as a function of frequency at various temperatures. Besides, in Fig. 9(a), the value of $M'$ is very low in the low frequency region for all the temperatures which indicate that the electrode polarization phenomenon makes a negligible contribution to $M^*$ and may be ignored when the electric data are analyzed in this form.[28,29] This observation may be related to a lack of restoring forces governing the mobility of charge carriers under the action of an induced electric field. This type of behavior supports the long-range mobility of charge carriers. As the frequency increases the value of $M'$ reaches a maximum corresponding to $M_\infty = (1/\varepsilon_\infty)$ at higher frequencies for all temperatures. In addition, in Fig. 9(b), $M''$ shows a slightly asymmetric peak at each temperature. The peak shifts towards higher frequencies and their maximum increases with the increasing temperature. The presence of such relaxation peaks in the $M''$ plots indicates that the samples are ionic conductors.[30] The region to the left of the peak is where the charge carriers are mobile over long distances while the region to the right is where they are spatially confined to the potential wells. The nature of modulus spectrum confirms the existence of a hopping mechanism in the electrical conduction of the material.[31] The variation of $M''/M''_{max}$ with $\omega/\omega_{max}$ at different temperatures is shown in

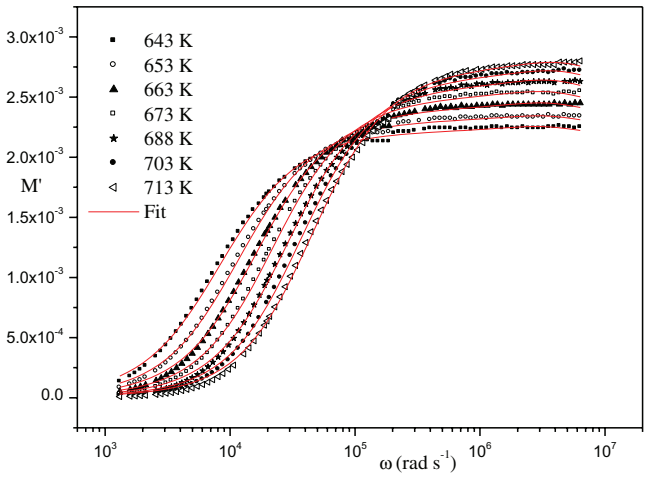


(a)

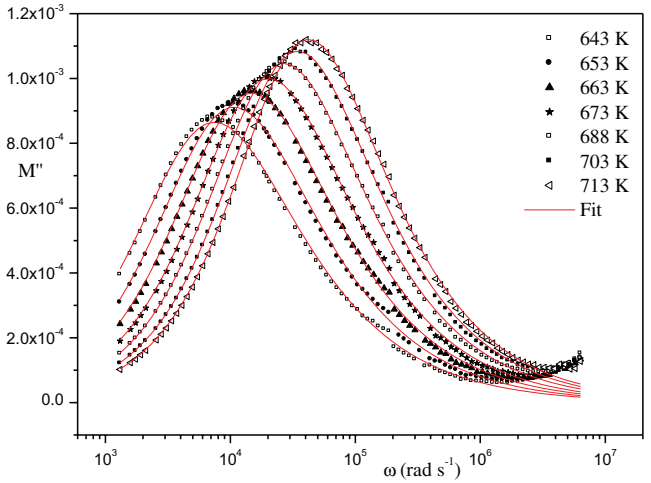


(b)

Fig. 9. Variation of $M'$ (a) and $M''$ (b) as a function of frequency at various temperatures of $Na_{0.9}Ba_{0.1}Nb_{0.9}$ $(Sn_{0.5}Ti_{0.5})_{0.1}O_3$.

Fig. 10, where $\omega_{max}$ is the angular frequency corresponding to $M''_{max}$. It shows the scaling behavior of the sample, where each $M''$ is scaled by $M''_{max}$ and each frequency axis is scaled by $\omega_{max}$. The perfect overlap of all the curves on a single master curve for all the temperatures suggests that the relaxation shows the same mechanism in the entire temperature range.[32]

The modulus plot can be characterized by the full width at half height or in terms of a nonexponential decay function.[33] The stretched exponential function is defined by the empirical Kohlrausch–Williams–Watts (KWW) function[34]:

$$\varphi(t) = \exp\left(-\left(\frac{t}{\tau}\right)^{\beta}\right) \quad 0 < \beta < 1, \tag{6}$$

where $\tau$ is the characteristic relaxation time and $\beta$ is the well-known Kohlrausch parameter, which decreases with an increase in the relaxation time distribution. The value of the

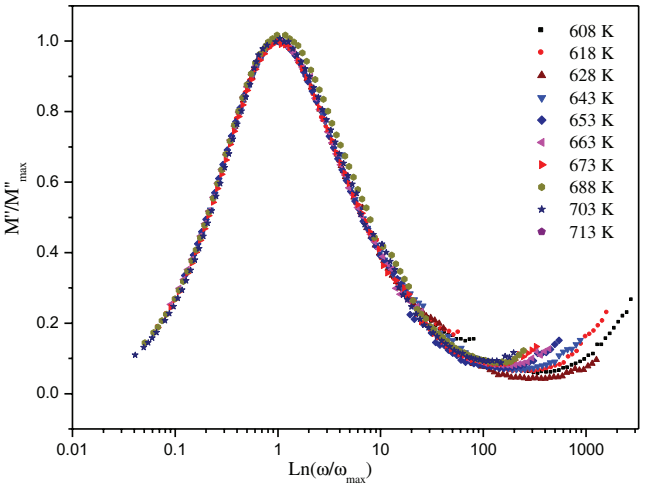


Fig. 10. Scaling behavior of Im($M$) of $Na_{0.9}Ba_{0.1}Nb_{0.9}$ $(Sn_{0.5}Ti_{0.5})_{0.1}O_3$ ceramic.

Kohlrausch parameter $\beta$ for a practical solid electrolyte is clearly less than 1, $\varphi(t)$ is related to the modulus in the angular frequency domain by the expression:

$$M = Ms\left[1-\int_0^{\infty} e^{-j\omega t}\left(-\frac{d\varphi(t)}{dt}\right)dt\right] = Ms[1-\varphi(\omega)]. \quad (7)$$

Among these functions, the Havriliak–Negami (HN) one has been the most extensively used in literature.[35,36] The HN function is

$$\phi_{HN}(\omega) = \frac{1}{[1+(i\omega\tau)^{\alpha}]^{\gamma}}, \quad (8)$$

where $\alpha$ and $\gamma$ are shape parameters ranging between 0 and 1. The Cole–Cole function corresponds to the case $0 < \alpha < 1$ and $\gamma = 1$ and the Cole–Davidson to $\alpha = 1$ and $0 < \gamma < 1$. The Debye case is recovered again with $\alpha = \gamma = 1$. Alvarez *et al.* established that for HN function which approximately corresponds to the Fourier transform of $d\phi/dt$, these two shape parameters, $\alpha$ and $\gamma$, are related as follows[37,38]:

$$\gamma = 1-0.812\ (1-\alpha)^{0.387} \quad (9)$$

being the corresponding relationship between $\beta$ and HN parameters given by

$$\beta = (\alpha\gamma)^{1/1.23}. \quad (10)$$

In the electrical modulus formalism, the Havriliak–Negami equation has the following form:

$$M' = M_{\infty}\left(1-\frac{A}{A^2+B^2}\right) \quad (11)$$

$$M'' = M_{\infty}\left(\frac{B}{A^2+B^2}\right) \quad (12)$$

where $A$, $B$, $C$, and $\Psi$ are given as follows:

$$A = 1+(\omega\tau)^{\alpha}\cos\left(\frac{\alpha\pi}{2}\right)+\frac{1}{2}(\gamma-1)\mathrm{Ln}(C)\left[1+(\omega\tau)^{\alpha}\cos\left(\frac{\alpha\pi}{2}\right)\right] + (\gamma-1)(\omega\tau)^{\alpha}\Psi\sin\left(\frac{\alpha\pi}{2}\right) \quad (13)$$

$$B = (\omega\tau)^{\alpha}\sin\left(\frac{\alpha\pi}{2}\right)+\frac{1}{2}(\gamma-1)\mathrm{Ln}(C)(\omega\tau)^{\alpha}\sin\left(\frac{\alpha\pi}{2}\right) - (\gamma-1)\left[1+(\omega\tau)^{\alpha}\Psi\cos\left(\frac{\alpha\pi}{2}\right)\right] \quad (14)$$

$$C = 1+(\omega\tau)^{2\alpha}+2(\omega\tau)^{\alpha}\cos\left(\frac{\alpha\pi}{2}\right) \quad (15)$$

$$\Psi = \mathrm{arctg}\left[\frac{(\omega\tau)^{\alpha}\sin\left(\frac{\alpha\pi}{2}\right)}{1+(\omega\tau)^{\alpha}\cos\left(\frac{\alpha\pi}{2}\right)}\right]. \quad (16)$$

Experimental data of $M'$ and $M''$ are simultaneously fitted using Eqs. (11) and (12). The results are plotted in Figs. 9(a) and 9(b) by a solid line. As a result, a good agreement is observed. For each temperature, the parameters $\alpha$, $\gamma$, and $\beta$ are obtained.

The values of $\beta$ obtained by this formalism are very close to those obtained from the full width-at-half-maximum of the $M''$ spectrum ($\beta = 1.14/\mathrm{FWHM}$). Figure 11 exhibits the $\beta$ parameter, calculated from Eq. (10), variations with temperatures. The $\beta$ parameter remains in the vicinity of $(0.74 \pm 0.08)$

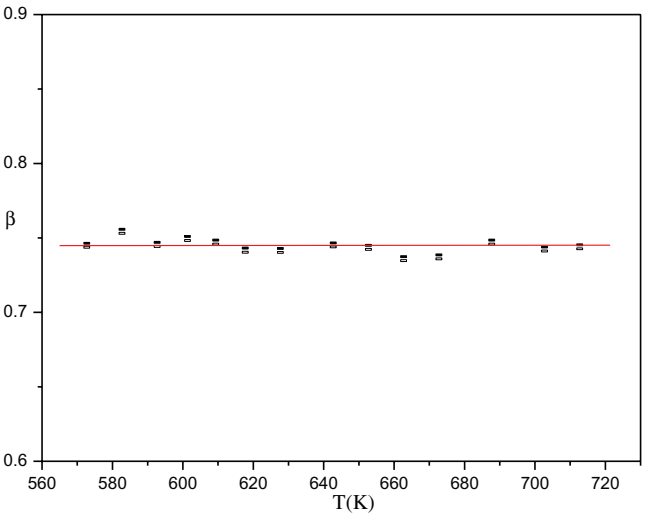


Fig. 11. Variation of $\beta$ as a function of temperature.

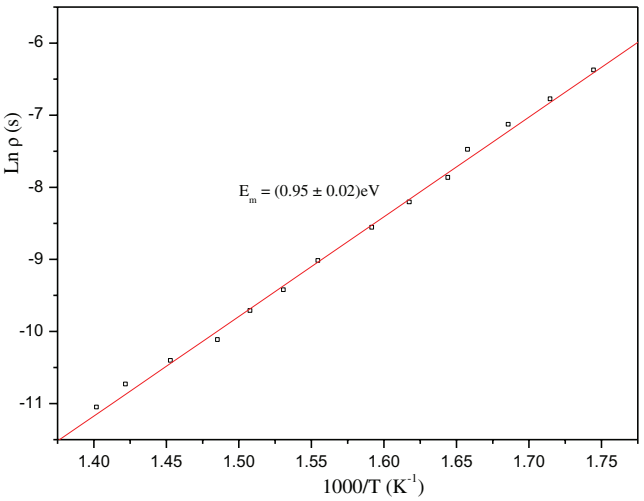


Fig. 12. Temperature dependence of relaxation time.

when the temperature varies. This suggests that all possible relaxation mechanisms occurring at different frequencies exhibit the same thermal energy and the dynamical processes are temperature independent.

The imaginary part of the modulus passes through a maximum at $\omega\tau = 1$ (Fig. 1(b)), where $\tau$ is the average electrical field relaxation time. The variation of the relaxation time $\tau$ with temperature follows the Arrhenius relation $\tau = \tau_0 \exp(E_m/kT)$, where $\tau_0$ is the characteristic relaxation time and $E_m = (0.95 \pm 0.04)$ is the activation energy (Fig. 12). The near value of activation energies obtained from the analyses of $M''$, conductivity data, and circuit equivalent confirm that the conductivity deduced from the impedance arcs is dominated by the grain-interior conductivity, i.e., characterized by the hopping of the ($O^{2-}$) ions in the material.[39]

## 4. Conclusion

In this work, the purity of prepared ceramic $Na_{0.9}Ba_{0.1}Nb_{0.9}(Sn_{0.5}Ti_{0.5})_{0.1}O_3$ was confirmed by X-ray powder diffraction. The electrical measurements show the appearance of semi-circular arcs, well modeled in terms of the equivalent electrical circuit. Besides, $Z'$ and $Z''$ curves merge above $10^5$ Hz at different temperatures reveals the reduced space charge polarization and contribution from grain. The scaling behavior of the imaginary part of the impedance implies that the relaxation shows the same mechanism in all the temperature range. The variation of ac conductivity with frequency has been observed to obey Jonscher's power law dependence. Indeed, the KWW function and the coupling model are used to analyze electric modulus at various temperatures. The near value of activation energies obtained from the analyses of modulus and conductivity data confirms that the transport is through ion hopping mechanism in the investigated material.

## References

[1]H. Sharma, S. Jindal and N. Aggarwal, Impact of copper doping on perovskite structure ferroelectric ceramic, *Mater. Today: Proc.* **33**, 1632 (2020).
[2]H. P. Uppara, H. Dasari, S. K. Singh, N. K. Labhsetwar and M. S. Murari, Effect of copper doping over $GdFeO_3$ perovskite on soot oxidation activity, *Catal. Lett.* **149**(11), 3097 (2019).
[3]S. Zhang, D. Guo, M. Wang, M. S. Javed and C. Hu, Magnetism in $SrTiO_3$ before and after UV irradiation, *Appl. Surf. Sci.* **335**, 115 (2015).
[4]M. V. Shisode, D. N. Bhoyar, P. P. Khirade and K. Jadhav, Structural, microstructural, magnetic, and ferroelectric properties of $Ba^{2+}$-doped $BiFeO_3$ nanocrystalline multifferroic material, *J. Supercond. Nov. Magn.* **31**, 2501 (2018).
[5]T. Xian, H. Yang, L. Di and J. Dai, Enhanced photocatalytic activity of $BaTiO_3$@ g-$C_3N_4$ for the degradation of methyl orange under simulated sunlight irradiation, *J. Alloys Compd.* **622**, 1098 (2015).
[6]P. P. Khirade, S. D. Birajdar, A. V. Humbe and K. Jadhav, Structural, electrical and dielectrical property investigations of Fe-doped $BaZrO_3$ nanoceramics, *J. Electron. Mater.* **45**, 3227 (2016).
[7]J. Wang, S. Jiang, D. Jiang, J. Tian, Y. Li and Y. Wang, Microstructural design of $BaTiO_3$-based ceramics for temperature-stable multilayer ceramic capacitors, *Ceram. Int.* **38**, 5853 (2012).
[8]D.-J. Shin, S.-J. Jeong, C.-E. Seo, K.-H. Cho and J.-H. Koh, Multi-layered piezoelectric energy harvesters based on PZT ceramic actuators, *Ceram. Int.* **41**, S686 (2015).
[9]R. Gautier, O. K. Anderson, P. Gougeon, J. F. Halet, E. Canadell and J. D. Martin, Electronic structure, electrical and magnetic properties of $RMo_8O_{14}$ compounds (R = La, Ce, Pr, Nd, Sm) containing bicapped $Mo_8$ clusters, *Inorg. Chem.* **41**, 4689 (2002).
[10]J. W. Liou and B. S. Chiou, Dielectric characteristics of doped $Ba_{1-x}Sr_xTiO_3$ at the paraelectric state, *Mater. Chem. Phys.* **51**, 59 (1997).
[11]W. Xiaoli and B. Li, Dielectric audio-frequency dispersion in $Ba(Ti_{1-x}Sn_x)O_3$ ferroelectrics, *J. Solid State Commun.* **149**, 537 (2009).
[12]V. V. Shvartsman, W. Kleemann and J. Dec, Diffuse phase transition in $BaTi_{1-x}Sn_xO_3$ ceramics: An intermediate state between ferroelectric and relaxor behavior, *J. Appl. Phys.* **99**, 124111 (2006).
[13]H. D. Magaw, The seven phases of sodium niobate, *Ferroelectrics* **7**, 87 (1974).
[14]H. Khelifi, A. Aydi, N. Abdelmoula, A. Simon, A. Maalej, H. Khemakhem and M. Maglione, Structural and dielectric properties of $Na_{1-x}Ba_xNb_{1-x}(Sn_{0.5}Ti_{0.5})_xO_3$ ceramics, *J. Mater. Sci.* **47**, 1943 (2012).
[15]C. Y. Hsu, H. Chou, B. Y. Liao and J. C. A. Huang, Magnetostriction studies in an antiferromagnetic polycrystalline $Mn_{42}Fe_{58}Mn_{42}Fe_{58}$ alloy, *Appl. Phys. Lett.* **89**, 262501 (2006).
[16]B. Shanmugavelu and V. V. Ravi, Thermal, structural and electrical studies of bismuth zinc borate glasses, *Solid State Sci.* **20**, 59 (2013).
[17]D. D. Macdonald, Reflections on the history of electrochemical impedance spectroscopy, *Electrochim. Acta* **51**, 1376 (2006).
[18]S. Selvasekarapandian and M. Vijaykumar, The ac impedance spectroscopy studies on $LiDyO_2$, *Mater. Chem. Phys.* **80**, 29 (2003).
[19]M. A. L. Nobre and S. Lanfredi, Dielectric properties of $Bi_3Zn_2Sb_3O_{14}$ ceramics at high temperature, *Mater. Lett.* **47**, 362 (2001).
[20]M. Ram, Role of grain boundary in transport properties of $LiCo_{3/5}Mn_{2/5}VO_4$ ceramics, *Phys. B: Phys. Condens. Matter* **405**, 602 (2010).
[21]B. Tiwari and R. N. Choudhary, Complex impedance spectroscopic analysis of Mn-modified Pb $(Zr_{0.65}Ti_{0.35})O_3$ electroceramics, *J. Phys. Chem. Solids* **69**, 2852 (2008).

[22]S. K. Barik, R. N. Choudhary and P. K. Mahapatra, Structural and electrical properties of $Na_{1/2}Gd_{1/2}TiO_3$ nanoceramics, *J. Alloys Compd.* **459**, 35 (2008).
[23]S. Saha and T. P. Sinha, Low-temperature scaling behavior of $BaFe_{0.5}Nb_{0.5}O_3$, *Phys. Rev. B* **65**, 134103 (2002).
[24]F. Yakuphanoglu, Y. Aydogdu, U. Schatzschneider and E. Rentschler, DC and AC conductivity and dielectric properties of the metal-radical compound: Aqua [bis (2-dimethylaminomethyl-4-NIT-phenolato)] copper (II), *Solid State Commun.* **128**, 63 (2003).
[25]R. H. Chen, R. Y. Chang and S. C. Shern, Dielectric and AC ionic conductivity investigations in K3H (SeO4) 2 single crystal, *J. Phys. Chem. Solids* **63**, 2069 (2002).
[26]P. S. Anantha and K. Hariharn, AC conductivity analysis and dielectric relaxation behaviour of NaNO3–Al2O3 composites, *Mater. Sci. Eng. B* **121**, 12 (2005).
[27]P. B. Macedo, C. T. Moynihan and R. Bose, The role of ionic diffusion in polarization in vitreous ionic conductors, *Phys. Chem. Glasses* **13**, 171 (1972).
[28]S. L. Agrawal, M. Singh, M. Tripathi, D. M. Mauli and K. Pandey, Dielectric relaxation studies on [PEO–$SiO_2$]: $NH_4SCN$ nanocomposite polymer electrolyte films, *J. Mater. Sci.* **44**, 6060 (2009).
[29]N. Hannachi, I. Chaabane, K. Guidara, A. Bulou and F. Hlel, AC electrical properties and dielectric relaxation of $[N(C_3H_7)_4]_2Cd_2Cl_6$, single crystal, *Mater. Sci. Eng. B* **172**, 2 (2010).
[30]V. Provenzano, L. P. Boesch, V. Volterra, C. T. Moynihan and P. B. Macedo, Electrical relaxation in $Na_2O \cdot 3SiO_2$ glass, *J. Am. Ceram. Soc.* **55**, 492 (1972).
[31]B. Behera, P. Nayak and R. N. P. Choudhary, Study of complex impedance spectroscopic properties of $LiBa_2Nb_5O_{15}$ ceramics, *Mater. Chem. Phys.* **106**, 193 (2007).
[32]S. Saha and T. P. Sinha, Low-temperature scaling behavior of $BaFe_{0.5}Nb_{0.5}O_3$, *Phys. Rev. B* **65**, 134103 (2002).
[33]K. P. Padmasree, D. K. Kanchan and A. R. Kulkarni, Impedance and modulus studies of the solid electrolyte system 20CdI2–80 [$xAg_2O$–$y$ (0.7 $V_2O_5$–0.3 $B_2O_3$)], where $1 \leq x/y \leq 3$, *Solid State Ionics* **177**, 475 (2006).
[34]B. Louati, K. Guidara and M. Gargouri, Dielectric and ac ionic conductivity investigations in the monetite, *J. Alloys Compd.* **472**, 347 (2009).
[35]S. Havriliak and S. Negami, A complex plane representation of dielectric and mechanical relaxation processes in some polymers, *Polymer* **8**, 161 (1967).
[36]J. C. Dyre, Source of non-Arrhenius average relaxation time in glass-forming liquids, *J. Non-Cryst. Solids* **235–237**, 142 (1998).
[37]F. Alvarez, A. Alegria and Colmenero, Relationship between the time-domain Kohlrausch-Williams-Watts and frequency-domain Havriliak-Negami relaxation functions, *J. Phys. Rev. B* **44**, 7306 (1991).
[38]F. Alvarez, A. Alegria and Colmenero, Interconnection between frequency-domain Havriliak-Negami and time-domain Kohlrausch-Williams-Watts relaxation functions, *J. Phys. Rev. B* **47**, 125 (1993).
[39]B. V. R. Chowdari and R. Gopalakrishnan, AC conductivity analysis of glassy silver iodomolybdate system, *Solid State Ionics* **23**, 225 (1987).